Comparative study on epsilon-near-zero transparent conducting oxides: High-order chromatic dispersions and modeling of ultrashort pulse interactions

Jiaye Wu [1], Ze Tao Xie [1], Yanhua Sha [1], H. Y. Fu [2], and Qian Li [1,*]

[1]*School of Electronic and Computer Engineering, Peking University, Shenzhen 518055, China*
[2]*Tsinghua-Berkeley Shenzhen Institute (TBSI), Tsinghua University, Shenzhen 518055, China*

A comparative study on the chromatic dispersions and the interactions with ultrashort pulses in epsilon-near-zero (ENZ) transparent conducting oxides (TCOs) is theoretically presented. The ENZ TCOs exhibit rapidly varying and unprecedentedly large Nth-order dispersions in the ENZ region, which is exclusive to ENZ plasmonic materials. However, it is found that in both physical and mathematical senses, the concepts of high Nth-order chromatic dispersions are inapplicable for ENZ TCOs with Drude-like permittivity. Subsequently, the impacts of the complex permittivity dispersion profiles on ultrashort pulse interactions are discussed. Comparisons are made between propagation patterns in an ENZ AZO waveguide obtained from the nonlinear Schrödinger equation (NLSE) and Maxwell's equations, as well as between interactions of femtosecond pulses with different temporal widths in a subwavelength ENZ AZO slab. Results show that the well-received NLSE is not suitable for modeling ENZ TCOs in either case, and subwavelength interaction patterns with different pulse widths are quite different, where the shorter pulse can excite stronger localized resonance.

I. INTRODUCTION

Epsilon-near-zero (ENZ) materials, with their capabilities to exhibit extraordinary optical properties within the region where the real part of the complex permittivity vanishes to zero, have attracted much scientific attention from various fields such as plasmonics, nonlinear optics, and nanophotonics [1–4]. The current state-of-the-art theoretical studies have unveiled optical properties of amplified electric fields [5], optical nonlinearity enhancement [6], directive emission of electromagnetic (EM) wave [7], ENZ mode [8,9], trapping of slow light [10], and dynamics of subwavelength quasi-standing-wave patterns [11].

Transparent conducting oxides (TCOs) such as indium tin oxide (ITO), gallium-doped zinc oxide (GZO), and aluminum-doped zinc oxide (AZO) are popular plasmonic materials to realized ENZ in the infrared regime. It has been found that in the proximity of the ENZ point, nonlinear effects such as ultrahigh Kerr nonlinearity [12,13] and harmonic generations [14–17] are found, and applications such as all-optical and electro-optical switching [18–20] are explored in ENZ TCOs.

In nonlinear optics, second-, third-, and high-order chromatic dispersions are important concepts in understanding nonlinear optical dynamics [21], which, however, are rarely discussed in ENZ materials. These chromatic dispersions are related to the refractive index which changes sharply due to the zero crossing of permittivity near the ENZ point. They could form high-order chromatic dispersions exclusive to ENZ materials, which is worth an in-depth discussion. Based

on the complex dispersion profile and optical nonlinearity, the modeling of ultrashort femtosecond pulse interactions with ENZ TCO materials can be further explored under longer-than-wavelength and subwavelength setups.

In this work, a comparative study is presented on the chromatic dispersions and the interactions with ultrashort pulses in ENZ TCOs. It is found that ITO, GZO, and AZO all exhibit rapidly varying and unprecedentedly large Nth-order dispersions in the ENZ region. However, resembling the situations in effective media metamaterials, near the ENZ wavelength, there exists the inapplicability of the high-order dispersion concept. This condition is reported and discussed in ENZ TCO materials under the Drude model. Subsequently, the impacts of the complex permittivity and refractive index dispersion profiles on ultrashort pulse interactions are analyzed. Comparisons are carried out between pulse propagation in an ENZ AZO waveguide simulated by the nonlinear Schrödinger equation (NLSE) and Maxwell's equations, as well as between light-matter interactions of femtosecond pulses with different temporal widths in a subwavelength ENZ AZO slab. It is shown that the well-received NLSE is not suitable for modeling ENZ TCOs in both cases due to different reasons, and the interaction patterns depend greatly on pulse widths, where the longer 100-fs pulse behaves like a pseudo-continuous-wave (pseudo-cw) which exhibits a more uniformly distributed electric field and excites weaker resonance, while the shorter 10-fs pulse can excite greater localized surface plasmon resonance (LSPR), indicating that temporal width might be another affecting factor of LSPR in ENZ TCOs. The findings of this work might be useful in broadening the understandings of light-matter interactions in ENZ materials.

This work is structured as follows. The high Nth-order chromatic dispersion profiles are discussed in Sec. II. The

---
*liqian@pkusz.edu.cn

comparison between NLSE and full Maxwell simulations on ultrashort pulse propagation is demonstrated in Sec. III, and the comparison of different-width pulse interactions with a subwavelength slab is discussed in Sec. IV. Finally, a conclusion of this article is drawn in Sec. V.

II. CHROMATIC DISPERSIONS OF TCOs

Although subtly engineered TCO nanostructures can exhibit non-Drude-like behavior [22], the complex permittivity of simple TCO slabs and nanolayers can still be precisely described by the Drude model [1–3,23],

$$\varepsilon_R = \varepsilon_r + i\varepsilon_i = \varepsilon_b - \frac{\omega_p^2}{(\omega^2 + \Gamma^2)} + i\frac{\omega_p^2\Gamma}{(\omega^2 + \Gamma^2)\omega}, \quad (1)$$

where ε_r and ε_i are the real and imaginary parts of the complex permittivity, and ω is the angular frequency of the EM wave. In this work, experimental data [1] for AZO [24], GZO [25], and ITO [26] are used. The high-frequency permittivity ε_b is 3.80 [1], and the damping rates Γ which represent the electron scattering rates are 9.710×10^{13} [1,24], 1.4929×10^{14} [1,25], and 1.2836×10^{14} rad/s [1,26] for AZO, GZO, and ITO, respectively. The plasmonic frequencies ω_p are tuned by free carrier concentration such that the ENZ points λ_{ENZ} where ε_r reach zero locate exactly at the telecom wavelength of 1550 nm, and their corresponding values are $\omega_p = 2.3765 \times 10^{15}$, 2.3867×10^{15}, and 2.3822×10^{15} rad/s, respectively. The variations of the complex permittivity are shown in Figs. 1(a) and 1(b). The refractive index $n + ik$ at this region can be calculated using the generalized Maxwell relations,

$$n = \sqrt{\frac{\sqrt{\varepsilon_r^2 + \varepsilon_i^2} + \varepsilon_r}{2}},$$
$$k = \frac{\varepsilon_i}{2n} = \sqrt{n^2 - \varepsilon_r}. \quad (2)$$

From Eq. (2), the intrinsic loss ε_i in TCO is generally nonzero and nontrivial. Therefore, no matter what value ε_r is,

n is always larger than zero. However, near λ_{ENZ}, n possesses values smaller than 1.0. The variations of the complex refractive index are plotted in Figs. 1(c) and 1(d). On the other hand, the attenuation coefficients α and α_{dB} can help one understand the degree of loss in ENZ TCOs more intuitively, which are defined as follows [21]:

$$\alpha(\omega) = \frac{\omega}{nc}\text{Im}[\chi^{(1)}(\omega)],$$
$$\alpha_{dB}(\omega) = 10(\log_{10}e)\alpha(\omega) \approx 4.343\alpha(\omega), \quad (3)$$

where $c = 299\,792\,458$ m/s is the speed of light in vacuum, and $\chi^{(1)}$ is the first-order susceptibility which can be obtained from $\varepsilon_R = 1 + \chi^{(1)}$. The dispersions of both attenuation coefficients are shown in Figs. 1(e) and 1(f).

From Fig. 1(a), the curves for the real part of the permittivity of the three TCOs are almost the same within the ENZ region. However, the values for intrinsic loss are quite different, as shown in Fig. 1(b), with AZO having the lowest loss. It is worth mentioning that, ε_b, ε_r, and ε_i may vary with different fabrication techniques and manufacturing errors, but the tendency would agree with Figs. 1(a) and 1(b). Compared with other TCOs, AZO tends to have a smaller Γ, meaning that the scattering rate of the electrons is relatively low, hence the lower optical loss. The same conclusion can be made from Figs. 1(d)–1(f) with k, α, and α_{dB}. However, even with AZO, at λ_{ENZ}, α_{dB} has a value of 0.0137 dB/nm, which means that in a $2\,\mu m$ propagation distance, the total linear loss is 27.48 dB at 1550 nm, indicating that ideally, only 0.18% of the incident power can transmit through. The huge loss limits the applications of ENZ TCOs in large-scale integrated photonic circuits and networks.

In Fig. 1(c), the curves of n experience a sharp turn near λ_{ENZ} due to the zero crossing of ε_r. In nonlinear optics, Nth-order dispersions are important concepts that greatly affect the interplay between nonlinearity, pulse chirp, and chromatic dispersion [27]. They are all derived from n-related propagation coefficient β [21], which is also known as the wave number. By incorporating the Drude model, the analytical expression of $\beta(\omega, \varepsilon_b, \omega_p, \Gamma)$ can be deduced as

$$\beta(\omega, \varepsilon_b, \omega_p, \Gamma) = \frac{n\omega}{c} = \frac{\sqrt{2}\omega}{2c}\sqrt{\varepsilon_b + \sqrt{\left(-\frac{\omega_p^2}{\Gamma^2 + \omega^2} + \varepsilon_b\right)^2 + \frac{\Gamma^2\omega_p^4}{\omega^2(\Gamma^2 + \omega^2)^2}} - \frac{\omega_p^2}{(\Gamma^2 + \omega^2)}}. \quad (4)$$

The Nth-order chromatic dispersions are defined as the coefficients of the Taylor expansion of β [21], namely, $\beta_N = d\beta^N/d^N\omega$. Each order of dispersion β_N denotes the ω-dependent dispersion of its previous order, β_{N-1}. If numerical derivatives are used to determine the values of β_N, one may find that with the increment of N, the curves of the high-order β_N will quickly become very inaccurate due to the loss of precision each order. Therefore, here we use analytical deductions to obtain higher-order dispersion values. In experiments, the Drude model is known to fit the measured permittivity very well in the ENZ region [3], and therefore we assume that the Drude function of Eq. (1) is the exact and actual

permittivity dispersion curve. By symbolic computation, the Drude-based analytical expressions for arbitrary order N can be calculated. The variations of β_1-β_4 for AZO, GZO, and ITO are plotted in Fig. 2 as examples.

Due to the physical nature of the drastically changing ε_r and n near λ_{ENZ}, and the mathematical nature of the square-root function in Eq. (4), ENZ TCOs, in theory, can have infinitive orders of nonzero rapidly varying dispersions. This dispersion profile is exclusive to ENZ materials in the ENZ region. For AZO, the maximum value of second-order dispersion is 0.2167 fs^2/nm at 1565.2 nm, which is one order of magnitude larger than the highly dispersive InP
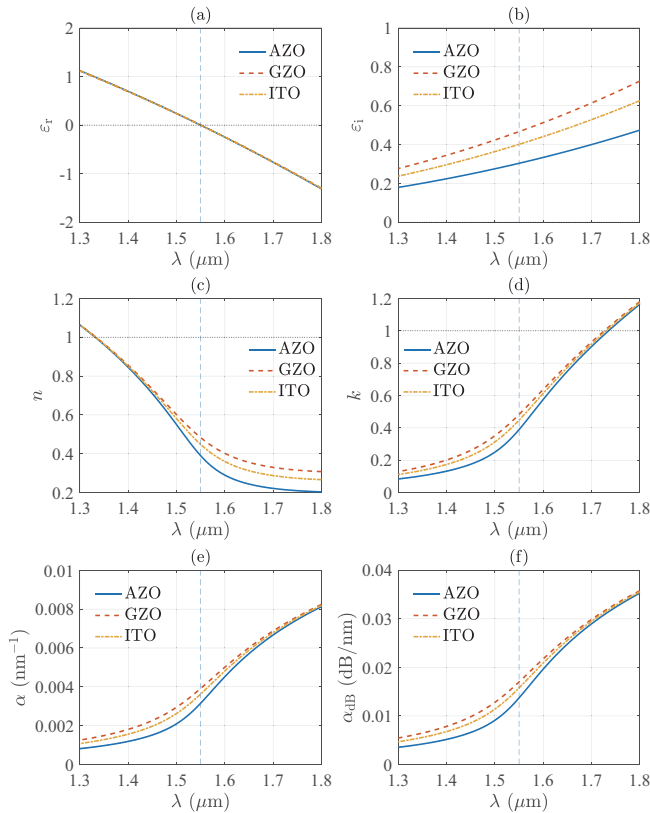
FIG. 1. The variations of the (a) real part of the permittivity ε_r, (b) imaginary part of the permittivity ε_i, (c) real part of refractive index n, (d) extinction coefficient k, (e) attenuation coefficient α, and (f) attenuation coefficient in decibel α_{dB} with wavelength. The solid, dashed, and dot-dashed lines represent AZO, GZO, and ITO, respectively.

FIG. 2. The variations of (a) first-order dispersion β_1, (b) second-order dispersion β_2, (c) third-order dispersion β_3, and (d) fourth-order dispersion β_4 with wavelength. The solid, dashed, and dot-dashed lines represent AZO, GZO, and ITO, respectively.

waveguide (~ 0.0296 fs^2/nm) [28], and several orders of magnitude larger than silica fibers (~ 20 ps^2/km) [21,27]. The maximum third-order dispersion is 3.2445 fs^3/nm, which is also significantly larger than silica fibers (~ 0.1 ps^3/km). It seems that these enormous values can be beneficial in designing efficient and nanoscale ENZ TCO-based dispersion compensators by the dispersion management technique [29]. However, the curves of the first four order dispersions in Figs. 2(a)–2(d) already indicate that in each order, the spectral locations for positive and negative maximum values do not always coincide and cancel each other out after dispersion management for any certain order. Seemingly, this complex high-order dispersion profile of ENZ TCOs renders their applications based on dispersion compensation almost impossible, while an even deeper reason lies behind its impracticality.

If higher orders of β_N are acquired in this way, it can be calculated that at 1550 nm, $\beta_4 = -324$ fs^4/nm, $\beta_5 = 1.23 \times 10^4$ fs^5/nm, $\beta_6 = 2.29 \times 10^6$ fs^6/nm, $\beta_7 = -9.77 \times 10^7$ fs^7/nm, $\beta_8 = -3.61 \times 10^{10}$ fs^8/nm, etc. These values do not decline with the increment of Taylor expansion order N, indicating that high-order chromatic dispersions defined at $\lambda_{ENZ} = 1550$ nm are problematic. Previously, the inapplicability of the high-order dispersion concepts has existed
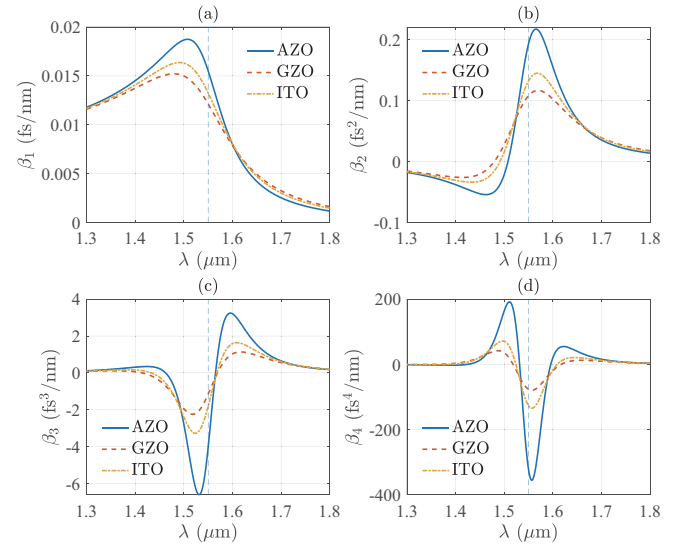
in metamaterials consisting of effective media or with an engineered "anomalous" permittivity profile [30–32]. Here, with analytical calculation, we found that this phenomenon also exists in ENZ TCOs with Drude-like permittivity at λ_{ENZ}. High orders of β_N are derived physical parameters other than the fundamental ones such as permittivity and the refractive index. This means that by their definitions they exist, but it is inappropriate to make the approximation in this case. The above comparisons of β_N between ENZ TCOs with other dielectric materials are therefore also questionable, as is their application of dispersion compensation. This poses another potential challenge in experiments because, in reality, the Nth-order dispersions of an optical material or product are not measured directly, but are calculated. They are, per se, parameters fitted by theoretical models, compared and approximated based on the measured results of pulse shapes, phase shifts, optical time-domain reflectometry, etc. Therefore, we consider that reporting the inapplicability of high-order dispersions in the ENZ regions of TCOs in this case is potentially useful and beneficial. As a result, the permittivity and refractive index of ENZ TCOs are relatively more reliable parameters to use in modeling. In Secs. III and IV, their impacts are further discussed under longer-than-wavelength and subwavelength setups.

III. PULSE PROPAGATION IN WAVEGUIDE LONGER THAN WAVELENGTH

As mentioned in Sec. II, due to the enormous intrinsic loss, waveguide lengths longer than 2 μm will result in spectral and temporal patterns too small to plot alongside the incident pulse as a comparison. Therefore, in this section, the propagation of an incident 100-fs full width at half maximum (FWHM) hyperbolic-secant pulse in a 2-μm-long ENZ AZO waveguide with an effective area of 0.64 μm^2 is discussed. ENZ AZO is chosen due to its relatively large dispersions and low loss, as

shown in Fig. 2. Due to the relations between dispersions, loss, and permittivity (or refractive index) [21], other ENZ TCO materials are expected to exhibit similar results as AZO. The behavior of the EM wave in nonlinear media is governed by Maxwell's equations:

$$\nabla \times \mathbf{H} = \frac{\partial \mathbf{D}}{\partial t},$$
$$\mathbf{D} = \varepsilon_0 \mathbf{E} + \mathbf{P},$$
$$\nabla \times \mathbf{E} = -\frac{\partial \mathbf{B}}{\partial t},$$
$$\mathbf{B} = \mu_0 \mathbf{H}, \qquad (5)$$

where $\mathbf{E}$ and $\mathbf{H}$ are electric and magnetic fields, and $\mathbf{D}$ and $\mathbf{B}$ are electric and magnetic inductions. The vacuum permittivity $\varepsilon_0 = 8.85 \times 10^{-12}$ F/m and the vacuum permeability $\mu_0 = 4\pi \times 10^{-7}$ N/A^2. Considering nonlinearity, the total polarization $\mathbf{P}$ induced by the electric dipoles is

$$\mathbf{P} = \varepsilon_0(\chi^{(1)} \cdot \mathbf{E} + \chi^{(2)} : \mathbf{EE} + \chi^{(3)} \vdots \mathbf{EEE}). \qquad (6)$$

Here, $\chi^{(2)}$ and $\chi^{(3)}$ are second- and third-order susceptibility, respectively. For the AZO waveguide, the experimental data [33] of $\chi^{(2)} = 3.87 \times 10^{-13}$ m/V and $\chi^{(3)} = 2.91 \times 10^{-22}$ m^2/V^2 are used. The Maxwell's Eqs. (5) and (6) can be solved numerically using the finite-difference time-domain (FDTD) method. In this work, simulations are run by commercially available software from LUMERICAL.

Alternatively, if a longer-than-wavelength optical structure is considered, whose length is significantly larger than the dimensions of its cross section and allows EM waves to propagate unidirectionally without considering the effects of multiple reflections and scattering, Eqs. (5) and (6) can be reduced to the well-received NLSE [21] which possesses the form

$$\frac{\partial A}{\partial z} + \frac{\alpha}{2}A - \sum_{N=1} \frac{i^{N+1}\beta_N}{N!} \frac{\partial^N A}{\partial t^N} - i\gamma|A|^2 A = 0, \qquad (7)$$

where $A(z, t)$ is the slow-varying envelope of the signal, and γ is the self-phase modulation coefficient which is related to $\chi^{(3)}$ by $\gamma = 3\pi\chi^{(3)}/(2\varepsilon_0 cn^2 \lambda S_{\text{eff}}) = 3.43$ W/m, with S_{eff} being the effective mode area. The attenuation coefficient $\alpha = 0.0137$ nm, as per Sec. II. It has also been discussed that the high values of high-order dispersions are unusable, but the existence of the higher-order effects can have a great impact on the pulse shape and spectrum. Therefore, the same approach as Ref. [34], i.e., subtracting the first two orders β_0 and β_1 from $\beta(\omega)$, is used here to express the dispersion terms in Eq. (7). This approach includes all effects of dispersion at $\lambda_{\text{ENZ}} = 1550$ nm without high-order Taylor expansion: $\tilde{\beta}(\omega) = \beta(\omega) - (\omega - \omega_0)\beta_1 - \beta_0$, where $\beta_0 = 1.5519 \times 10^{-17}$ nm, and $\beta_1 = 0.0155$ fs/nm.

The incident light for the Maxwell's Eqs. (5) is a 100-fs hyperbolic-secant pulse with a rapidly oscillating electric field. It has the form $u(0, t) = A(0, t)\cos(\omega_0 t)$, where $A(0, t) = \sqrt{P_0}\text{sech}(t/T_0)$ is the exact envelope mentioned in Eq. (7) and the very input signal for the NLSE. ω_0 is the corresponding angular frequency of the center wavelength, and P_0 is the peak power which is set to $P_0 = |\beta_2|/\gamma T_0^2$ in order to maintain a soliton state at the moment of incidence. T_0
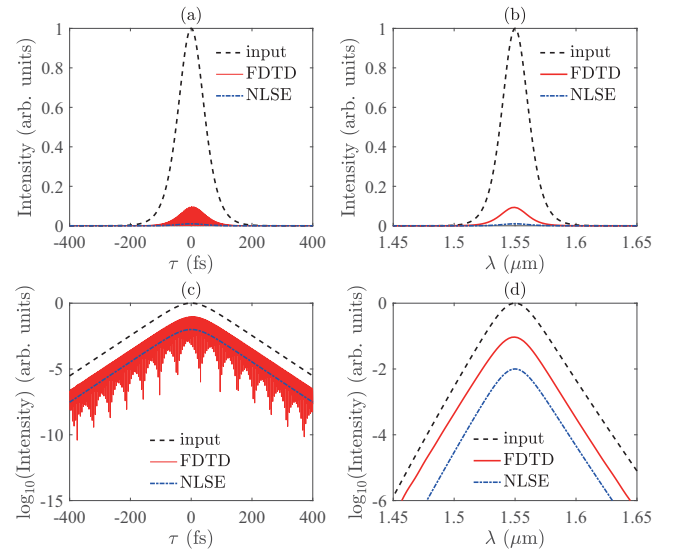

FIG. 3. Comparison of pulse propagation results in an ENZ AZO waveguide obtained from the NLSE and FDTD. The (a) linear and (c) logarithmic scales of the temporal shapes; the (b) linear and (d) logarithmic scales of the spectra. The dashed lines denote the envelope of the slow-varying input signal in (a) and (c), and its corresponding spectrum in (b) and (d). The solid and dot-dashed lines are results from FDTD and NLSE, respectively.

is the temporal width at $1/e$ intensity. The FWHM $T_{\text{FWHM}} = 2\ln(1 + \sqrt{2})T_0 \approx 1.763T_0 = 100$ fs. For this width, the corresponding $P_0 = 17.48$ kW, which is realizable by solid-state lasers. The propagation results obtained by Maxwell's equations (via FDTD) and the NLSE are shown in Fig. 3 as solid and dot-dashed lines, respectively.

As can be seen from Figs. 3(a) and 3(b), the 100-fs pulse suffers from significant loss. The linear loss is predicted to be ∼99.82%, with only ∼0.18% of energy transmitted, based on the α value at 1550 nm from Sec. II. In Fig. 3, the results from NLSE agree with this linear loss prediction because the corresponding α_{dB} value at 1550 nm is used as a global value for all considered wavelengths in the NLSE simulation. However, in Figs. 1(d)–1(f), the loss is not uniform across the ENZ region. The average loss in 1300–1700 nm can be estimated by $\bar{\alpha}_{\text{dB}} = \int \alpha_{\text{dB}}(\lambda)d\lambda/\Delta\lambda = 0.0124$ dB/nm, which is smaller than the value at 1550 nm, while NLSE assumes the same loss across the considered range. Also, Eq. (7) only considers the effects of $\chi^{(3)}$ in the form of Kerr nonlinearity, and it does not take into account the effects of sum-frequency generation of $\chi^{(2)}$. Therefore, the energy redistribution processes are different between the results of NLSE and FDTD. This means that in this case, in the ENZ region, it appears that NLSE tends to overestimate the total loss, while FDTD yields a loss that is smaller than linear prediction, and their difference is within one order of magnitude. Due to the discrepancy of these two methods in handling loss, in other scenarios (not limited to the case presented here), the NLSE can either overestimate or underestimate the actual loss when the loss curve is not flat in the considered region. In Figs. 3(c) and 3(d), the two methods maintain the typical "triangular" feature of hyperbolic-secant function in the logarithmic scale, but the central wavelength of

the NLSE result blueshifts to 1549 nm. These results indicate that although, with a complex permittivity profile, ENZ TCOs might be able to support pulse propagation, its significantly high loss greatly limits its application in long waveguide structures.

Conclusively, with a complex dispersion and attenuation profile, the NLSE results are generally similar to full Maxwell simulations, which might provide fast evaluations because the FDTD method is very time consuming. However, the latter directly take complex permittivity into its calculations, which inherently includes possible leakage, scattering, and all orders of dispersions and attenuation values for different wavelengths, whose results are, in theory, closer to reality. Although the NLSE is sufficiently accurate for normal dielectric waveguide structures, it is not recommended for the simulation of ENZ TCO materials with complicated dispersion and attenuation profiles.

IV. PULSE INTERACTIONS WITH SUBWAVELENGTH STRUCTURES

In the regime of nanophotonics, especially in ENZ materials, the multiple reflections and scattering of light can play a big role in forming linear and nonlinear dynamics. Therefore, in subwavelength structures, the NLSE is no longer valid due to its approximation limits. Therefore, under the subwavelength setup, all calculations should be carried out by full Maxwell simulation. From previous works [11], one knows that complex spectral and temporal patterns can be created in subwavelength ENZ TCO slabs, which are mixed results of multiple reflections, scattering, and the interplay between high dispersion and high nonlinearity. However, the impact of the temporal widths of ultrashort pulses has not been reported.

In this section, the interactions of a 100-fs and a 10-fs hyperbolic-secant pulse with a 250-nm-thick ENZ AZO slab are analyzed. The thickness of the slab is $\sim 1/6$ of the incident wavelength and the cross section of the slab is 800×800 nm. As an attempt to maintain the pulse shape, the fundamental soliton condition in Sec. III is used, P_0 is 17.48 kW for the 100-fs pulse and 1.75 MW for the 10-fs pulse, which are all possible with the state-of-the art solid-state lasers [12,17,21]. The pulses are launched into the slab along the 250-nm-long axis [shown as the z axis in Figs. 4(e) and 4(f)] and the incident end is marked "0 nm," while the exit end is marked "250 nm." Due to the existence of potential reflections, scattering, and resonance, the temporal and spectral profiles that are recorded are a combined result of different processes. The temporal and spectral profiles for the 100-fs pulse are plotted in Figs. 4(a) and 4(c), while those for the 10-fs pulse are plotted in Figs. 4(b) and 4(d). To investigate the differences between the two interaction processes, the schematic diagrams of the normalized electric-field distribution patterns obtained from the trailing-edge wavelengths of the corresponding pulses are demonstrated in Figs. 4(e) and 4(f), respectively, with the green rectangles marking the boundary of the subwavelength ENZ AZO slab, and the incident direction along the z axis from $z = 125$ to $z = -125$. The reasons for studying the electric-field distributions from the pulses' spectral edges are that they are pulse-width related and
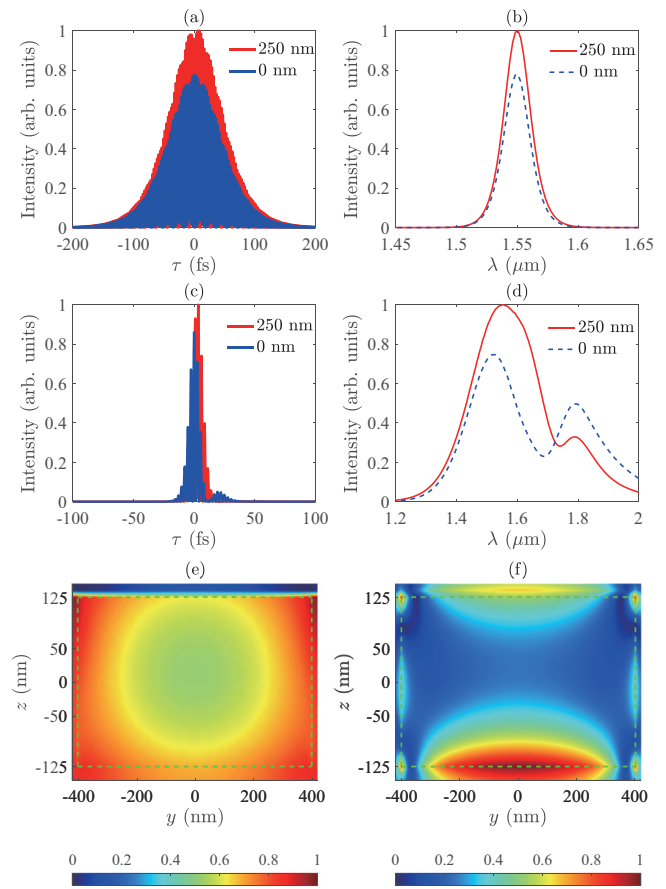

FIG. 4. Comparison of the subwavelength ENZ AZO slab interactions with 100-fs and 10-fs pulses. (a), (c) The temporal and spectral profiles of the 100-fs pulse. (b), (d) The corresponding diagrams of the 10-fs pulse. In (a)–(d), the blue lines denote the profiles obtained at the incident end, and the red lines are the profiles obtained at the opposite end. (e), (f) The schematic diagrams of the electric-field distribution from the pulses' spectral edges for the 100-fs and 10-fs pulse, respectively. The green dashed rectangles in (e) and (f) mark the boundary of the ENZ AZO slab.

the 10-fs group exhibits a distinctive pattern that is not found in the 100-fs group by adjusting the wavelength of interest.

Comparing with the 10-fs pulse, the 100-fs pulse acts like a pseudo-cw wave. As can be seen from Figs. 4(a) and 4(c), both the 0-nm and the 250-nm temporal and spectral profiles do not show significant change. The temporal and spectral peak power is larger at the 250-nm than at the 0-nm mark due to the on-site reflection at the AZO-air interface (the reflected waves are attenuated and become much weaker when they return to the 0-nm mark). From Fig. 4(e), the EM energy propagates around the ENZ AZO slab, with relatively low portion entering and interacting with the material. The electric-field distribution is relatively uniform and even. The 0-nm mark corresponding to $(y, z) = (0, 125)$ in Fig. 4(e) is at the inner edge of the wrap-around electric field, whose strength is apparently weaker than the 250-nm mark $(y, z) = (0, -125)$, which is located at the middle to the outer edge of the electric field. Also, at the 250-nm mark, there exists a very small area of energy localization, indicating some type of resonance.

In subwavelength plasmonic ENZ materials, it is common to find LSPR at the plasma-air interfaces. At the nanoscale, the wavelength and strength of the LSPR are related to the material's shape, size, and nanostructure composition (dopant concentration), and the ambient media's optical properties [1,2,35–37]. Particularly, in gold nanorods and silver nanoparticles, the LSPR can be related to wavelength and bandwidth [38,39]. A similar phenomenon is suspected in ENZ TCOs, and the electric-field energy localization at the 250-nm mark in Figs. 4(a) and 4(c) might be LSPR, but it is not very significant in Fig. 4(e).

In the 10-fs pulse case, the presented interaction patterns are completely different. From Figs. 4(b) and 4(d), multiple peaks appear alongside the main pulse, both in temporal and spectral profiles. This might be due to the interplay between higher-order dispersions and nonlinearity and, considering the high linear reflection [11] in longer wavelengths, the EM waves recorded at the 0-nm mark generally have a longer optical distance, hence the accumulated effects of frequency conversion and the splitting of the main pulse lead to the stronger secondary peak. The changes in spectral widths are due to redistribution of energy and adiabatic frequency conversion in the ENZ region below and above the band gap [40]. The electric-field distribution in Fig. 4(f) shows multiple resonances at the four surfaces and corners, with the 250-nm mark $(y, z) = (0, -125)$ being the strongest. These resonances are clearly the LSPRs, and their incident direction dependency indicates that the excited patterns resemble the situation in a Kretschmann-Raether configuration. The stronger LSPR at the 250-nm mark than at the 0-nm mark explains the corresponding higher power in Figs. 4(b) and 4(d). In reality, considering the ultrashort duration of the 10-fs pulse compared to the 100-fs one, we speculate that another physical process might be involved which could cause different types of pulse-matter interactions: it is called a "nonthermal process" [41–43], where the Drude model is still able to describe the complex permittivity of the material, but the lattice temperature does not change under the 10-fs pulse excitation. Only the free carrier density around the Fermi level is redistributed. This circumstance is due to the longer relaxation time than the pulse duration. Normally, after the free carriers are elevated to the conduction band via intraband absorption [40,44], they will relax by a scattering processes of ∼100 fs [40,45], which is much longer than the 10-fs pulse. This is why the actual pulse-matter interactions of the 10-fs and 100-fs pulse might be significantly different.

Additional simulations show that if the P_0 value for the 100-fs pulse (17.48 kW, 100 times weaker) is chosen for the 10-fs pulse regardless of the fundamental soliton condition, the interaction pattern (electric-field distribution pattern) remains basically the same with Fig. 4(f), except for the 100-times-weaker resonance intensity. This indicates that the enormous difference between the 100-fs and the 10-fs results is related to the temporal width of the pulse, not the peak power.

In conclusion, the interaction dynamics for 100-fs and 10-fs pulses are totally different. The 100-fs pulse induced a more evenly distributed electric field and a significantly weaker resonance. The temporal and spectral profiles remain almost unchanged. On the other hand, the 10-fs pulse shows a significant change in both temporal and spectral profiles, and

it excites a much stronger LSPR at the exit end of the slab by a different physical process. These results might indicate that besides shape, size, and composition, the temporal width of the incident pulse can be another determining factor of the LSPR in ENZ TCOs.

V. CONCLUSIONS

In this work, a comparative study on the Nth-order chromatic dispersions and the interactions with ultrashort pulses in ENZ TCOs is presented. Exclusive to ENZ plasmonic materials, ITO, GZO, and AZO exhibit rapidly varying and unprecedentedly large Nth-order dispersions in the ENZ region. However, resembling the situations in effective media, the concepts of the high-order dispersions are found to be inapplicable in the proximity of the ENZ wavelength for both physical and mathematical reasons, and the uses of complex permittivity and refractive index in describing the dispersion of ENZ TCOs are highly advisable.

Subsequently, the influences of the complicated and novel dispersion profile on ultrashort pulse interactions under different setups are discussed. A comparison is made between propagation patterns in an ENZ AZO waveguide obtained from the NLSE and Maxwell's equation by the FDTD method. It is found that the NLSE is not suitable for modeling such materials due to its incapability to include the wavelength dependency of chromatic dispersions and attenuation, which are not negligible in ENZ TCO materials. Also, modeling subwavelength materials is beyond the approximation limit of the NLSE; therefore, considering multiple reflections, scattering, and resonance, full Maxwell simulations using the FDTD method are performed for such structures.

Another comparison is made between interactions with 100-fs and 10-fs ultrashort pulses in a subwavelength ENZ AZO slab. Results show that the interaction patterns and mechanisms are fundamentally different, and the 100-fs pulse acts like a pseudo-cw wave with a more evenly distributed electric field and a significantly weaker resonance. The temporal shape and the spectrum of the shorter 10-fs pulse are altered dramatically, and greater LSPR can be excited, which might reveal the temporal-width dependency of the LSPR in ENZ TCO nanostructures.

The issues and problems discussed in this work regarding the inapplicability of higher-order dispersions and ultrashort pulse interaction modeling might also be applicable in metal-insulator multilayered ENZ materials [46,47], for they are a combination of effective media and nanostructures. The results of this work can be beneficial in broadening the understanding of light-matter interaction dynamics in ENZ materials.

[1] G. V. Naik, V. M. Shalaev, and A. Boltasseva, Adv. Mater. **25**, 3264 (2013).

[2] X. Niu, X. Hu, S. Chu, and Q. Gong, Adv. Opt. Mater. **6**, 1701292 (2018).

[3] I. Liberal and N. Engheta, Nat. Photon. **11**, 149 (2017).

[4] N. Kinsey, C. DeVault, A. Boltasseva, and V. M. Shalaev, Nat. Rev. Mater. **4**, 742 (2019).

[5] S. Campione, D. de Ceglia, M. A. Vincenti, M. Scalora, and F. Capolino, Phys. Rev. B **87**, 035120 (2013).

[6] A. Ciattoni, C. Rizza, A. Marini, A. D. Falco, D. Faccio, and M. Scalora, Laser Photon. Rev. **10**, 517 (2016).

[7] S. Enoch, G. Tayeb, P. Sabouroux, N. Guérin, and P. Vincent, Phys. Rev. Lett. **89**, 213902 (2002).

[8] S. Vassant, J.-P. Hugonin, F. Marquier, and J.-J. Greffet, Opt. Express **20**, 23971 (2012).

[9] S. Campione, I. Brener, and F. Marquier, Phys. Rev. B **91**, 121408(R) (2015).

[10] A. Ciattoni, A. Marini, C. Rizza, M. Scalora, and F. Biancalana, Phys. Rev. A **87**, 053853 (2013).

[11] J. Wu, B. A. Malomed, H. Y. Fu, and Q. Li, Opt. Express **27**, 37298 (2019).

[12] M. Z. Alam, I. De Leon, and R. W. Boyd, Science **352**, 795 (2016).

[13] L. Caspani, R. P. M. Kaipurath, M. Clerici, M. Ferrera, T. Roger, J. Kim, N. Kinsey, M. Pietrzyk, A. Di Falco, V. M. Shalaev, A. Boltasseva, and D. Faccio, Phys. Rev. Lett. **116**, 233901 (2016).

[14] A. Capretti, Y. Wang, N. Engheta, and L. Dal Negro, ACS Photon. **2**, 1584 (2015).

[15] T. S. Luk, D. de Ceglia, S. Liu, G. A. Keeler, R. P. Prasankumar, M. A. Vincenti, M. Scalora, M. B. Sinclair, and S. Campione, Appl. Phys. Lett. **106**, 151103 (2015).

[16] L. Rodríguez-Suné, M. Scalora, A. S. Johnson, C. Cojocaru, N. Akozbek, Z. J. Coppens, D. Perez-Salinas, S. Wall, and J. Trull, APL Photon. **5**, 010801 (2020).

[17] Y. Yang, J. Lu, A. Manjavacas, T. S. Luk, H. Liu, K. Kelley, J.-P. Maria, E. L. Runnerstrom, M. B. Sinclair, S. Ghimire, and I. Brener, Nat. Phys. **15**, 1022 (2019).

[18] N. Kinsey, C. DeVault, J. Kim, M. Ferrera, V. M. Shalaev, and A. Boltasseva, Optica **2**, 616 (2015).

[19] Q. Guo, Y. Cui, Y. Yao, Y. Ye, Y. Yang, X. Liu, S. Zhang, X. Liu, J. Qiu, and H. Hosono, Adv. Mater. **29**, 1700754 (2017).

[20] Z. T. Xie, J. Wu, H. Y. Fu, and Q. Li, IEEE Photon. J. **12**, 4501510 (2020).

[21] G. P. Agrawal, in *Nonlinear Fiber Optics*, 5th ed., edited by G. P. Agrawal (Academic Press, Oxford, 2013).

[22] C.-L. Pan, C.-S. Yang, R.-P. Pan, P. Yu, and G.-R. Lin, *Terahertz Spectroscopy–A Cutting Edge Technology* (InTech, Rijeka, Croatia, 2017).

[23] P. Drude, Ann. Phys. **306**, 566 (1900).

[24] H. Agura, A. Suzuki, T. Matsushita, T. Aoki, and M. Okuda, Thin Solid Films **445**, 263 (2003).

[25] S.-M. Park, T. Ikegami, and K. Ebihara, Thin Solid Films **513**, 90 (2006).

[26] S. Ray, R. Banerjee, N. Basu, A. K. Batabyal, and A. K. Barua, J. Appl. Phys. **54**, 3497 (1983).

[27] J. Wu and Q. Li, J. Opt. **21**, 085503 (2019).

[28] J. O. Kjellman, R. Stabile, and K. A. Williams, J. Lightwave Technol. **35**, 3791 (2017).

[29] N. Smith, N. Doran, W. Forysiak, and F. Knox, J. Lightwave Technol. **15**, 1808 (1997).

[30] B. E. A. Saleh and M. C. Teich, *Fundamentals of Photonics*, 1st ed. (Wiley, New York, 1991).

[31] P. A. Belov, R. Marqués, S. I. Maslovski, I. S. Nefedov, M. Silveirinha, C. R. Simovski, and S. A. Tretyakov, Phys. Rev. B **67**, 113103 (2003).

[32] F. Capolino, *Theory and Phenomena of Metamaterials* (CRC Press, Boca Raton, FL, 2010).

[33] W. Tian, F. Liang, S. Chi, C. Li, H. Yu, H. Zhang, and H. Zhang, ACS Omega **5**, 2458 (2020).

[34] J. M. Dudley and J. R. Taylor, in *Supercontinuum Generation in Optical Fibers*, 1st ed., edited by J. M. Dudley and J. R. Taylor (Cambridge University Press, Cambridge, 2010).

[35] K.-S. Lee and M. A. El-Sayed, J. Phys. Chem. B **110**, 19220 (2006).

[36] J. B. González-Díaz, A. García-Martín, J. M. García-Martín, A. Cebollada, G. Armelles, B. Sepúlveda, Y. Alaverdyan, and M. Käll, Small **4**, 202 (2008).

[37] E. Hutter and J. H. Fendler, Adv. Mater. **16**, 1685 (2004).

[38] F. Kusa and S. Ashihara, J. Appl. Phys. **116**, 153103 (2014).

[39] J. Doster, G. Baraldi, J. Gonzalo, J. Solis, J. Hernandez-Rueda, and J. Siegel, Appl. Phys. Lett. **104**, 153106 (2014).

[40] J. B. Khurgin, M. Clerici, V. Bruno, L. Caspani, C. DeVault, J. Kim, A. Shaltout, A. Boltasseva, V. M. Shalaev, M. Ferrera, D. Faccio, and N. Kinsey, Optica **7**, 226 (2020).

[41] R. Rosei, Phys. Rev. B **10**, 474 (1974).

[42] N. Del Fatti, C. Voisin, M. Achermann, S. Tzortzakis, D. Christofilos, and F. Vallée, Phys. Rev. B **61**, 16956 (2000).

[43] G. Della Valle, M. Conforti, S. Longhi, G. Cerullo, and D. Brida, Phys. Rev. B **86**, 155139 (2012).

[44] H. Wang, K. Du, C. Jiang, Z. Yang, L. Ren, W. Zhang, S. J. Chua, and T. Mei, Phys. Rev. Appl. **11**, 064062 (2019).

[45] N. Kinsey and J. Khurgin, Opt. Mater. Express **9**, 2793 (2019).

[46] J. Kuttruff, D. Garoli, J. Allerbeck, R. Krahne, A. De Luca, D. Brida, V. Caligiuri, and N. Maccaferri, Commun. Phys. **3**, 114 (2020).

[47] A. R. Rashed, B. C. Yildiz, S. R. Ayyagari, and H. Caglayan, Phys. Rev. B **101**, 165301 (2020).